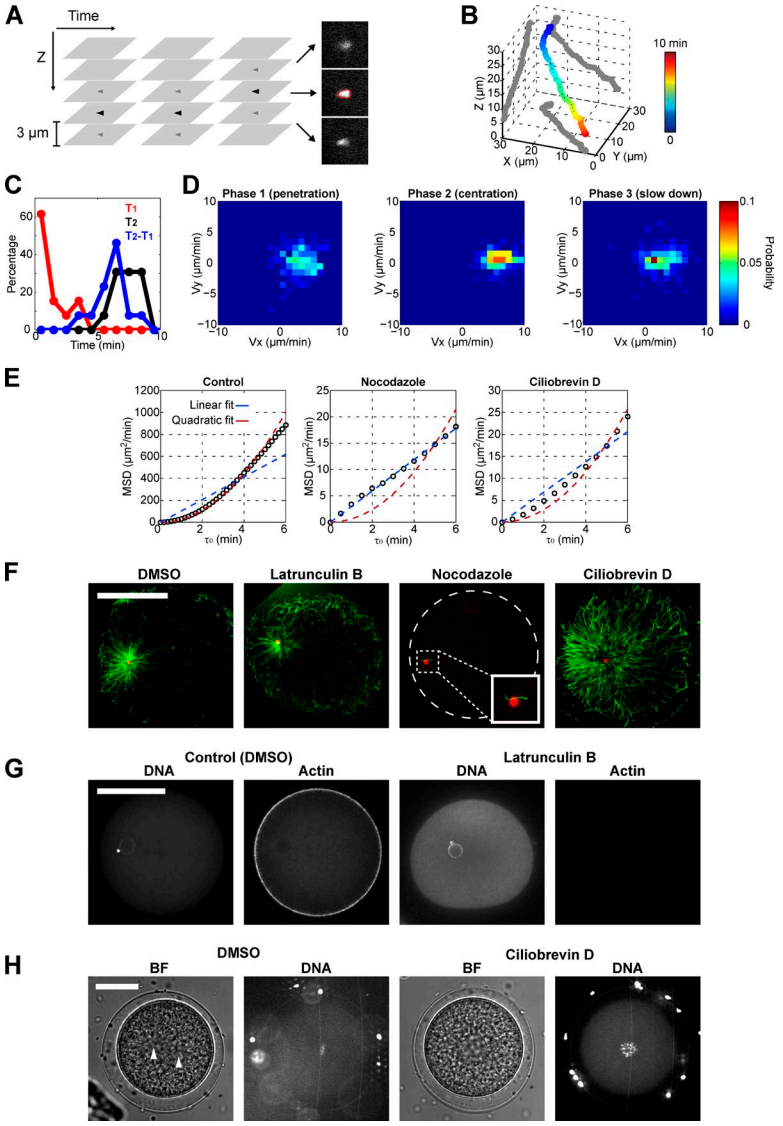

Figure S1. **Method for aster 3D tracking, extended characterization of aster centration dynamics, and effects of various inhibitors on MTs and actin organization.** (A and B) Method for 3D aster tracking. (A) Sperm pronuclei are imaged at each time point by acquiring 15 confocal z-slices spaced by an interval of 3 µm. The mid z-position is then automatically selected by finding the plane with maximal Hoechst signal. (B) The high Z resolution tracking confirms that asters migrate straight in 3D. Time is color coded. (C) Probability density function of T_1, T_2, and $T_1 - T_2$ (period of phase 2) obtained from $n = 13$ cells. Note that the PDF of $T_2 - T_1$ is narrower than that of T_1 and T_2, suggesting the duration of the centering phases is rather constant between cells though the time when it starts may vary more. (D) Probability density function of aster instantaneous in-plane velocity vectors for the migration three phases. The coordinates were defined so that the x axis connects sperm entry point and cell center. (E) Mean square displacement (MSD) of asters in normal conditions and in the presence of 20 µM nocodazole and 50 µM ciliobrevin D (see Materials and methods). The MSDs are the mean of $n = 13$ (control), $n = 7$ (nocodazole), and $n = 6$ (ciliobrevin D) cells. Broken lines indicate linear (blue) and quadratic (red) fits. The control data were well fitted by a quadratic function indicating a uniform centration with constant speed. In contrast, nocodazole data were fitted well by linear function indicating random diffusion. The MSD of ciliobrevin D–treated asters was not well fitted by a linear or quadratic function, suggesting a weakly biased random motion. The speed of normal centration computed from this MSD analysis ($MSD(\tau) = A\tau^2$, $V = \sqrt{A}$) is 5.2 µm/min, similar to the speed determined from a linear fitting of the traveling distance curve (5.3 µm/min). (F) MT aster immunostaining performed in the presence of DMSO (control), latrunculin B, nocodazole, and ciliobrevin D. Drug assays are performed as in Fig. 1 (F–I) and cells are fixed 3 min after drug addition. (G) F-Actin staining in the presence/absence of latrunculin B. The same image intensity range is used for phalloidin staining in control and latrunculin B–treated cells. (H) Effects of ciliobrevin D on mitotic spindle bipolarity. DMSO (control) and ciliobrevin D were added 60 min postinsemination (between prophase and metaphase), and cells were imaged 10 min after. Control cells exhibit a normal spindle bipolar organization and chromosome plate alignment, whereas ciliobrevin D–treated cells display disorganized chromosomes.

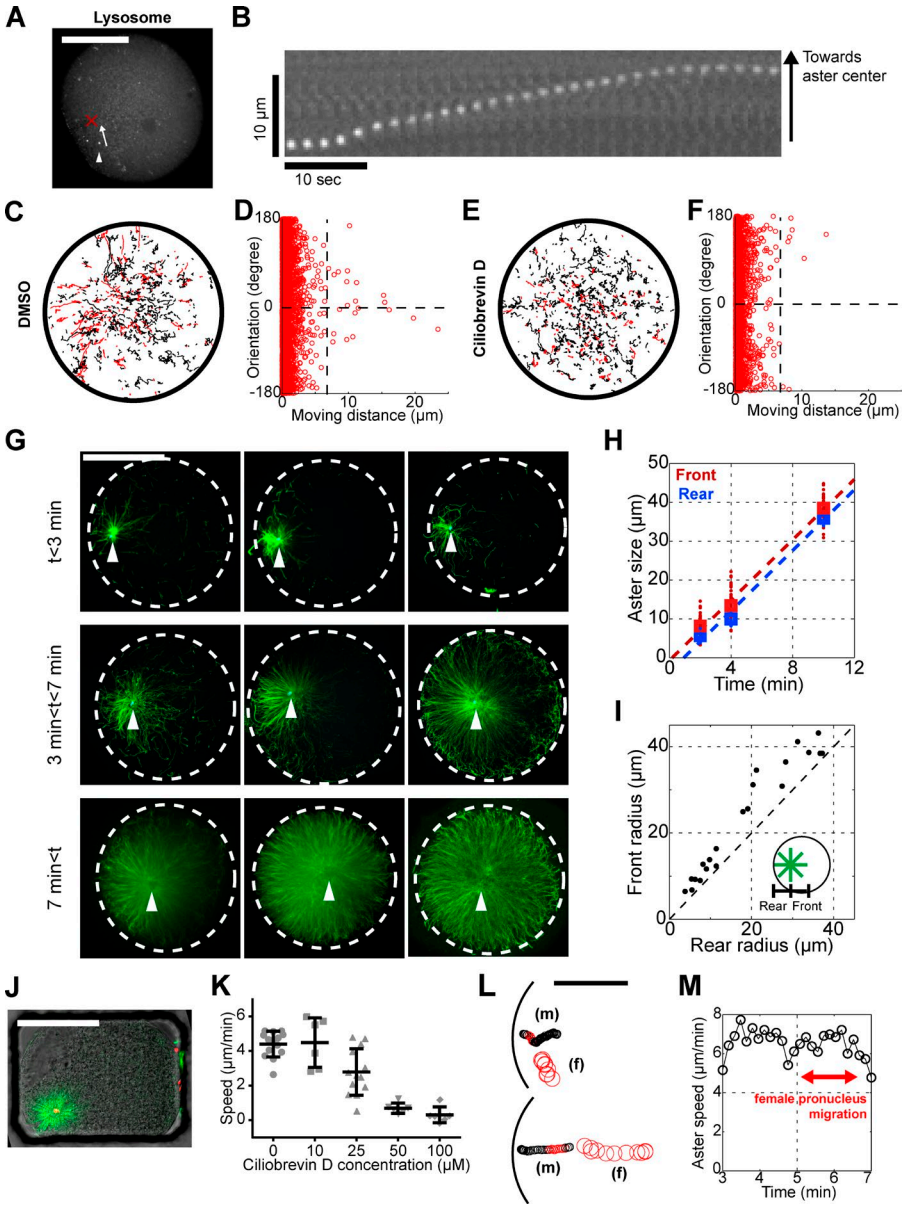

Figure S2. **Effects of ciliobrevin D on vesicle trafficking, growth of sperm MT asters, dose-dependent effects of ciliobrevin D on aster speed, and influence of the female pronucleus on sperm aster speed and trajectories.** (A and B) Lysosome movements. (A) Lysosome vesicles stained with LysoTracker are imaged every 1 s during a whole centration process. (B) Kymograph highlighting a rapid centripetal lysosome motion toward the aster center along a length of more than 10 µm, at a speed of ~0.5 µm/s. The vesicle tracked is highlighted by the white arrowhead in A. (C–F) Quantification of lysosome movement. (C and E) Superimposition of all tracked trajectories of lysosomes during a 10 min movie after fertilization in eggs treated with DMSO (C) or with 50 µM ciliobrevin D (E). Red trajectories correspond to lysosome movements within ±20° toward the aster center. (D and F) Scatterplot of lysosome motion orientation plotted as a function of their traveled distance. Ciliobrevin D treatment abolishes most persistent centripetal vesicle motion within the plane of focus. (G) Time-dependent immunostaining of growing and centering sperm MT asters (MTs are in green and aster centers are indicated with white arrowheads). The indicated time is taken in reference with sperm entry by accounting for a mean 3-min delay between sperm addition and sperm entry into the egg. Note the absence of MT–cortex contact at timings before 7 min (H) Aster growth rate estimation. Mean aster size is computed from immunostaining images of several eggs fixed at different time points after sperm entry. Both front and rear radius growth rate are estimated from the slope of the linear fit indicated by the dotted lines, which yields an estimate of 3.8 µm/min. (I) Aster shape asymmetry is computed by comparing front and rear radii of asters images obtained from 21 individual stained eggs at various times. More than 10 individual astral MTs (or bundles) are analyzed for each aster front to compute front radius, and the rear radius is defined as the distance between the aster center and the nearest cell cortex. The dotted line marks the symmetry axis for aster shapes. The plot suggests that the shape asymmetry is ~5 to 10 µm and mostly independent of aster absolute size. Immunostaining used for both H and I was performed in PDMS channel, which flattens slightly the eggs in Z, to maintain centration in the plane. (J) Sperm MT aster in a rectangular-shaped egg visualized by in situ immunostaining. (K) Dose-dependent effects of ciliobrevin D concentration on aster speed. The assay and quantification is performed as in Fig. 1 (F–I). Note that for 10 µM, asters show a transient slow down followed by a speed recovery (Fig. 4, G–I). (L and M) Effects of female pronucleus (marked with large red dots) movement on aster centration (small dots) dynamics. The female pronucleus starts migrating toward aster center presumably when contacting astral MTs. (L) The small black dots mark the aster center before or after female pronucleus movement; the small red dots correspond to the period when the female pronucleus in moving. In rare cases, the female pronucleus position is initially close to the sperm entry point and begins migration soon after fertilization, when the sperm aster is small and bends the aster trajectory (L, top). In most cases, the female pronucleus position is initially far from sperm entry point, and the female starts moving when the sperm aster is already large enough and does neither influence sperm aster trajectory and speed (L, bottom; and M). Error bars represent SD. Bars, 50 µm.

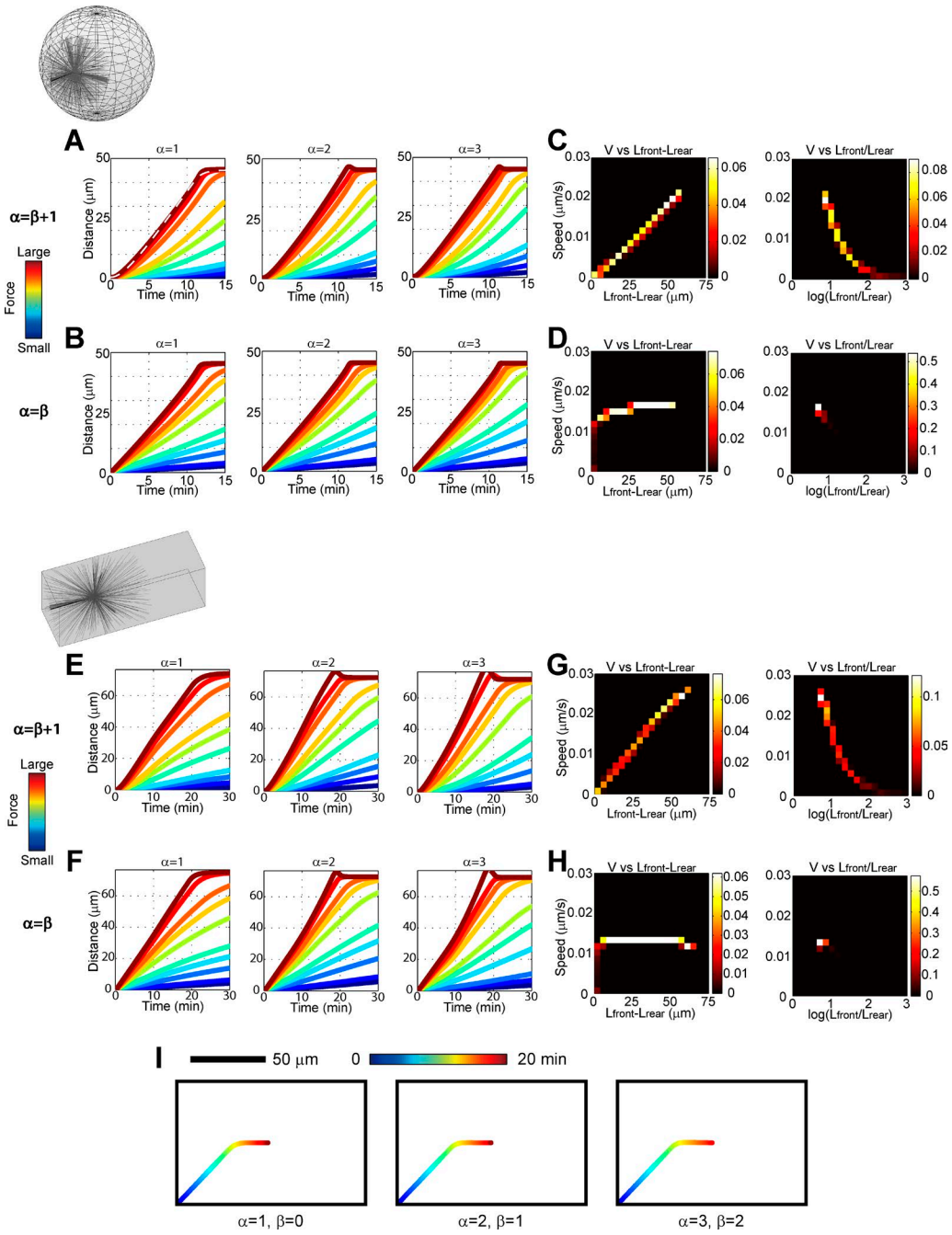

Figure S3. **3D numerical simulations testing the influence of scaling exponents and cell shape on aster speed.** (A) Simulations of aster distance–time plots for α = 1, 2, 3 and $\alpha = \beta + 1$ were performed for a spherical boundary condition. Colors in distance–time plots indicate the amplitude of the force parameter a/b. The white dotted line in the left (α = 1) correspond to the result of the analytical solution of the 1D model with adjusting a/b (Eq. 11). (B) Simulations of aster distance-time plots for α = 1, 2, 3 and $\alpha = \beta$; colors in distance–time plots indicate the amplitude of the force parameter a/b. (C) Density plots of aster instantaneous speed against $L_{front} - L_{rear}$ and L_{front}/L_{rear} obtained for α = 1 and β = 0 and relatively small values of the force parameter a/b. Note that this density plot was produced from a single simulation run containing more than 9,000 data points (the same for D, G, and H). (D) Density plots of aster instantaneous speed against $L_{front} - L_{rear}$ and L_{front}/L_{rear} obtained for α = 1 and β = 1 and relatively small values of the force parameter a/b. (E–H) 3D numerical simulations using the same parameter assays as in A–D, but in a 3D rectangular shape. (I) Trajectories of sperm asters obtained from 3D numerical simulation obtained using different values of scaling exponents, as indicated.

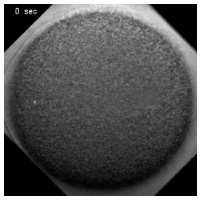

Video 1. **Sperm MT aster centration in a normal spherical shape cell.** Male pronucleus of fertilized sea urchin egg was visualized using DNA dye Hoechst. DIC (gray) and Hoechst (cyan) images were obtained by time-lapse spinning-disk confocal microscopy (Ti-Eclipse [Nikon] combined with CSU-X1 spinning head [Yokogawa]). Frames were taken every 10 s (shown every 2 frames) for 15 min.

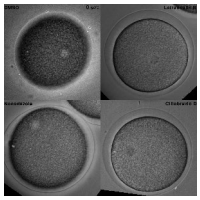

Video 2. **Aster centration in the presence of various inhibitors.** Aster centration in the presences of 1% DMSO (top left), 20 µM Latrunculin B (top right), 20 µM Nocodazole (bottom left), 50 µM Ciliobrevin D (bottom right). DIC (gray) and Hoechst (cyan) images were obtained by time-lapse spinning-disk confocal microscopy (Ti-Eclipse [Nikon] combined with CSU-X1 spinning head [Yokogawa]). Frames were taken every 30 s for 20 min.

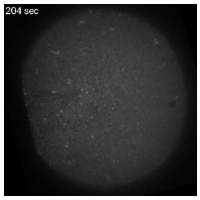

Video 3. **Lysosome dynamics during aster centration.** Lysosome vesicle trafficking during pronuclear migration in the presence of 1% DMSO was visualized with LysoTracker dye. Images were obtained by time-lapse spinning-disk confocal microscopy (Ti-Eclipse [Nikon] combined with CSU-X1 spinning head [Yokogawa]). Frames were taken every second (shown every six frames) for 10 min.

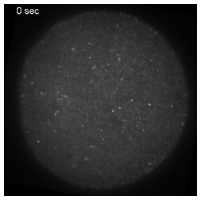

Video 4. **Lysosome dynamics in the presence of 50 µM ciliobrevin D.** Lysosome vesicle trafficking during pronuclear migration visualized with LysoTracker dye. Addition of 50 µM ciliobrevin D in the course of the time lapse is indicated with the red text. Images were obtained by time-lapse spinning-disk confocal microscopy (Ti-Eclipse [Nikon] combined with CSU-X1 spinning head [Yokogawa]). Frames were taken every second (shown every six frames) for 10 min.

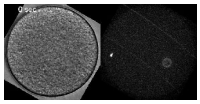

Video 5. **Laser ablation of a centering MT aster 1: side ablation.** Sperm aster motion is monitored before and after photoablation along the red dotted line. DIC (left) and Hoechst (right) images were obtained by time-lapse spinning-disk confocal microscopy (Ti-Eclipse [Nikon] combined with CSU-X1 spinning head [Yokogawa]). Frames were taken every 30 s for 17 min.

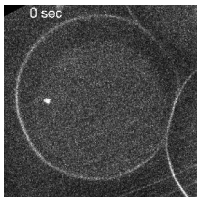

Video 6. **Laser ablation of a centering MT aster 2: front ablation.** Sperm aster motion is monitored before and after photo-ablation along the red dotted line. DIC (left) and Hoechst (right) images were obtained by time-lapse spinning-disk confocal microscopy (Ti-Eclipse [Nikon] combined with CSU-X1 spinning head [Yokogawa]). Frames were taken every 10 s for 17 min.

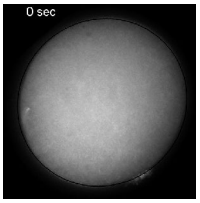

Video 7. **Live MT aster dynamics visualized with injected fluorescent tubulin.** The MT aster was visualized by injecting fluorescent tubulin solution. Images were obtained by time-lapse spinning-disk confocal microscopy (Ti-Eclipse [Nikon] combined with CSU-X1 spinning head [Yokogawa]). Frames were taken every 30 s for 17 min.

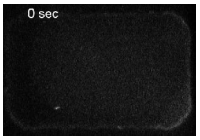

Video 8. **Aster centration in a rectangular-shaped egg.** Aster centration in a rectangular-shaped egg was visualized using DNA dye Hoechst. Images were obtained by time-lapse spinning-disk confocal microscopy (Ti-Eclipse [Nikon] combined with CSU-X1 spinning head [Yokogawa]). Frames were taken every 10 s for 15 min.

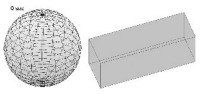

Video 9. **3D Numerical simulation of an aster centering in normal spherical and rectangular geometries.** Numerical simulations of a 3D model for normal spherical cell geometry (left) and for a rectangular cell geometry (right). The spherical cell has a radius of 45 μm. The rectangular-shaped cell dimensions are [width, depth, height] = [144, 48, 55] in μm. In the rectangular geometry simulation, the aster starts at the corner in the midplane. 1/50 of total MTs are shown. Frames were taken every 10 s (100 simulation steps) for 25 min.

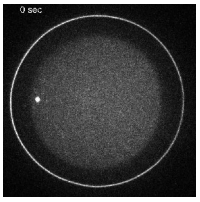

Video 10. **Aster centration in the presence of 10 μM ciliobrevin D.** Sperm aster motion is filmed before and after treatment with 10 μM ciliobrevin D using DNA dye Hoechst. Images were obtained by time-lapse spinning-disk confocal microscopy (Ti-Eclipse [Nikon] combined with CSU-X1 spinning head [Yokogawa]). Frames were taken every 30 s for 17 min.